

## Supporting Information for Role of the monovalent cation on the self-doping of tin halide perovskites

Isabella Poli,<sup>1\*</sup> Edoardo Albanesi,<sup>2,3</sup> Cesare Boriosi,<sup>3,4</sup> Corinna Ponti,<sup>5,6</sup> Luca Gregori,<sup>4,7</sup> Giovanna Bruno,<sup>4</sup> Daniele Meggiolaro,<sup>7</sup> Pietro Rossi,<sup>3</sup> Antonella Treglia,<sup>3</sup> Davide Ruzza,<sup>5,6</sup> Paola Delli Veneri,<sup>5</sup> Lucia V. Mercaldo,<sup>5</sup> Antonio Abate,<sup>6,8,9</sup> Mario Caironi,<sup>3</sup> Filippo De Angelis,<sup>4,7,10</sup> and Annamaria Petrozza<sup>3\*</sup>

1. Center for Sustainable Future Technologies@Polito, Istituto Italiano di Tecnologia, Via Livorno, 60, Turin, 10144 Italy
2. Department of Industrial Chemistry "Toso Montanari", University of Bologna, Via Piero Gobetti 85, Bologna, 40129 Italy
3. Center for Nano Science and Technology@Polimi, Istituto Italiano di Tecnologia, via Rubattino 81, Milano, 20134 Italy
4. Department of Chemistry, Biology and Biotechnology, University of Perugia, Via Elce di Sotto 8, Perugia, 06123 Italy
5. Italian National Agency for New Technologies, Energy and Sustainable Economic Development (ENEA), Portici Research Center, Piazzale Enrico Fermi 1, Portici (NA), 80055 Italy
6. Department of Chemical Materials and Industrial Production Engineering, University of Naples Federico II, Napoli, Piazzale Tecchio 80 Italy
7. Computational Laboratory for Hybrid/Organic Photovoltaics (CLHYO), Istituto CNR di Scienze e Tecnologie Chimiche (SCITEC-CNR), Via Elce di Sotto 8, Perugia, 06123 Italy
8. Helmholtz-Zentrum Berlin für Materialien und Energie, Kekuléstraße 5, 12489 Berlin, Germany
9. Department of Chemistry Bielefeld University, Universitätsstraße 25, 33615 Bielefeld, Germany
10. SKKU Institute of Energy Science and Technology (SIEST) Sungkyunkwan University, Suwon 440-746, South Korea

### Materials and Methods

**Materials** - N,N-dimethylformamide (DMF, anhydrous, 99.8%), dimethyl sulfoxide (DMSO, anhydrous, ≥99.9%) Anisole (anhydrous, 99.7%), Tin(II) iodide (AnhydroBeads, -10 mesh, 99.99%) was purchased from Sigma-Aldrich. Formamidinium iodide (FAI) and methylammonium iodide (MAI) were purchased by Greatcellsolar Materials. Cesium Iodide (CsI, 99.999%) was purchased by Alfa Aesar. All chemicals were used without any further purification. ITO coated glass and glass substrates were cleaned in acetone and isopropyl alcohol (IPA) for 10 min by sonication. The cleaned substrates were treated with oxygen plasma for 10 min before any further deposition. Thin-film perovskite deposition was done in a N<sub>2</sub>-filled glovebox.

### Methods

#### *Spin coated perovskites*

**FASnI<sub>3</sub> perovskite:** A stock solution of FASnI<sub>3</sub> was first prepared by mixing FAI:SnI<sub>2</sub> in the molar ratio of 1:1, and then dissolved in DMF/DMSO mixed solvents (4:1 v/v) to form solutions 1.2 M. When specified, 10mol% with respect to SnI<sub>2</sub> content was added to the precursor solution. The "non-optimized" perovskite films were prepared by spin coating the perovskite precursor solution at 4000 rpm for 50 s. 80 μL of Anisole was spun onto the spinning substrate after 25 seconds (antisolvent dripping). The perovskite films were

then annealed at 120 °C for 15 min on the hot plate in the N<sub>2</sub> filled glovebox. The deposition process was then optimized to improve the morphology of the films. Full coverage thin films were prepared by spin coating the perovskite precursor solution at 1000 rpm for 10 seconds and 4000 rpm for 40 s. 80 μL of Anisole was spun onto the spinning substrate after 25 seconds (antisolvent dripping). The perovskite films were then left at 5 minutes at room temperature and then annealed at 120 °C for 15 min on the hot plate in the N<sub>2</sub> filled glovebox.

MASnI<sub>3</sub> perovskite: A stock solution of MASnI<sub>3</sub> was first prepared by mixing MAI:SnI<sub>2</sub> in the molar ratio of 1:1, and then dissolved in DMF/DMSO mixed solvents (4:1 v/v) to form solutions 1.2 M. When specified, 10mol% with respect to SnI<sub>2</sub> content was added to the precursor solution. The “non-optimized” perovskite films were prepared by spin coating the perovskite precursor solution at 4000 rpm for 50 s. 80 μL of Anisole was spun onto the spinning substrate after 25 seconds (antisolvent dripping). The perovskite films were then annealed at 120 °C for 15 min on the hot plate in the N<sub>2</sub> filled glovebox. The deposition process was then optimized to improve the morphology of the films. Full coverage thin films were prepared by spin coating the perovskite precursor solution at 1000 rpm for 10 seconds and 4000 rpm for 40 s. 80 μL of Chlorobenzene kept at 60°C was spun onto the spinning substrate after 25 seconds (antisolvent dripping with hot antisolvent<sup>1</sup>). The perovskite films were then annealed at 100 °C for 15 min on the hot plate in the N<sub>2</sub> filled glovebox.

CsSnI<sub>3</sub> perovskite: A stock solution of CsSnI<sub>3</sub> was first prepared by mixing CsI:SnI<sub>2</sub> in the molar ratio of 1:1, and then dissolved in DMF/DMSO mixed solvents (4:1 v/v) to form solutions 1.2 M. When specified, 10mol% with respect to SnI<sub>2</sub> content was added to the precursor solution. The “non-optimized” perovskite films were prepared by spin coating the perovskite precursor solution at 4000 rpm for 50 s. 80 μL of Anisole was spun onto the spinning substrate after 25 seconds (antisolvent dripping). The perovskite films were then annealed at 120 °C for 15 min on the hot plate in the N<sub>2</sub> filled glovebox. The deposition process was then optimized to improve the morphology of the films. Full coverage thin films were prepared by spin coating the perovskite precursor solution at 1000 rpm for 10 seconds and 4000 rpm for 40 s. A stream of N<sub>2</sub> was sprayed toward the spinning wet film during the spin-coating process after 25 seconds and left flowing for the 10 seconds. Then the perovskite films were then annealed at 150 °C for 15 min on the hot plate in the N<sub>2</sub> filled glovebox.

#### *Evaporated perovskites*

Thermally evaporated CsSnI<sub>3</sub> thin films were deposited using a Kenosistec Evaporation System integrated in a N<sub>2</sub> filled glove box. The films were deposited on glass/ITO substrates previously cleaned and treated with UV-ozone for 25 minutes. The two precursors were evaporated as received, as beads. Once the substrates were positioned in the vacuum chamber, the power of the sources (two Knudsen cells, each one equipped with its own Quartz Crystal Microbalance) was activated only when a vacuum level of 10<sup>-7</sup> mbar was reached. The SnI<sub>2</sub> source temperature was set to a nominal value of 270°C obtaining a real deposition rate of 0.17 Å/s while for the CsI source the nominal temperature was 530 °C corresponding to a real deposition rate of 0.22 Å/s. The two materials were sequentially evaporated, maintaining the substrate rotation at 10 rpm, always starting with the SnI<sub>2</sub> layer and finishing with the CsI layer: for double layer samples (DL) just one cycle of evaporation was carried out, while for multilayers (ML) 10 cycles of thinner layers were executed. In all cases the deposition times were adjusted to have a ratio between the total thicknesses SnI<sub>2</sub>/CsI equal to 0.85, which corresponds to a molar ratio equal to 1, and a final film thickness of 300 nm. Once concluded the evaporation procedure, the samples were annealed at 170 °C for 5 min on a hot plate in the N<sub>2</sub> filled glovebox.

#### **Characterization**

**UV-Vis Absorption** Absorption spectra were measured on perovskite thin films deposited on glass using a UV/VIS spectrophotometer Lambda 1050, PerkinElmer, in the wavelength range 500–1100 nm, with step size of 1 nm. Samples were glass encapsulated right after fabrication in a N<sub>2</sub> filled glovebox by means of a UV-curable epoxy edge sealant (LED401, Masterbond) to avoid air degradation prior and during analysis.

**XRD** patterns were recorded with a Bruker D8 Advance diffractometer with Bragg–Brentano geometry equipped with a Cu K $\alpha$ 1 ( $\lambda = 1.544060$  Å) anode, operating at 40 kV and 40 mA. The diffraction patterns were collected at room temperature, with a step size of 0.05 in symmetric scan reflection mode and an acquisition time of 2 s. XRD patterns were recorded on thin films deposited on glass substrates and loaded onto a Bruker airtight specimen holder in a N<sub>2</sub> filled glovebox to avoid air contamination during the measurement.

**PL** Steady state PL was measured by exciting the thin film with an unfocused beam of a 450 nm c.w. diode laser (Oxxius). Photoluminescence was collected in reflection mode at a right angle from the excitation line and focused into a fiber coupled to a spectrometer (Ocean Optics Maya Pro 2000) with an intensity of  $\approx 100$  mW cm<sup>-2</sup>. PL was measured in air on glass encapsulated samples. PLQY was measured by using a femtosecond laser (Light Conversion Pharos) with a repetition rate of 500 kHz. The laser was directed onto the sample surface, and the photoluminescence was captured through a two-lens system. The pump fluences were adjusted using a gradual neutral density filter wheel, and the size of the irradiated spot was changed to achieve the lowest excitation density. The relative photoluminescence quantum yield (PLQY) is calculated by spectrally integrating the photoluminescence signal and dividing it by the corresponding excitation density. All samples were glass encapsulated in a N<sub>2</sub> filled glovebox right after fabrication by means of a UV-curable epoxy edge sealant (LED401, Masterbond) to avoid air degradation prior and during analysis.

**SEM** images were obtained using a MIRA3 TESCAN microscope with an accelerating voltage of 5 kV. Perovskite films were prepared on ITO substrates. The samples were loaded onto SEM pin stubs inside the glovebox and placed onto a multi holder. The holder was transferred to the microscope using an airtight transfer tube, which was opened only when the SEM specimen chamber was evacuated to quickly transfer the holder with samples in the microscope chamber and evacuate the chamber. The transfer time to the microscope was measured to be under 30 seconds, ensuring minimal oxidation.

**Hall effect** measurements were obtained using a Hall effect measurement system (semiautomatic) (HMS5300, Ecopia) using Van Der Pauw method with constant current source and 0.56 Tesla permanent magnet. Thin films were deposited onto ITO patterned substrates with the four electrical contacts in the corners. All samples were glass encapsulated in a N<sub>2</sub> filled glovebox right after fabrication by means of a UV-curable epoxy edge sealant (LED401, Masterbond) to avoid air degradation prior and during analysis.

**Conductivity** was measured using a four-point resistivity probe (Hand Applied Probe, Jandel Engineering Limited, Bridge Technology) with 1 mm distance between each point, coupled with a Portable Four Point Prober Test Meter (HM21). The films were deposited on glass and the conductivity was measured in the glovebox right after deposition. **Computational details**

Defects have been simulated in the 2x2x2 supercells of the MASnI<sub>3</sub>, FASnI<sub>3</sub> and CsSnI<sub>3</sub> phases by using the Perdew-Burke-Ernzherof (PBE) functional<sup>3</sup> and including DFT-D3 dispersion.<sup>4</sup> For all the phases the lattice parameters have been fixed to the experimental valued,  $a = b = 8.758$  Å,  $c = 12.429$  Å,  $a = b = 8.838$  Å,  $c = 12.407$  Å,  $a = 8.689$  Å,  $b = 8.638$  Å,  $c = 12.378$  Å, for MASnI<sub>3</sub>, FASnI<sub>3</sub>, CsSnI<sub>3</sub> respectively.<sup>5-7</sup> DFT calculations have been carried out by using norm-conserving pseudopotentials (pseudo dojo repository,<sup>8</sup> explicitly included shells: Sn 4s, 4p, 4d, 5s, 5p; I 5s, 5p; N, C 2s, 2p; H 1s; Cs 5s 5p 6s) a cutoff of 60 Ry for the wavefunctions and by sampling the Brillouin zone at the Gamma point.

To model the alloying of  $\text{FASnI}_3$  with 25% of MA and Cs we first relaxed both the lattice parameters of  $\text{FASnI}_3$  unit cell and the atomic positions before and after cation substitutions. When employing norm-conserving pseudopotential to relax also the cell parameters, a plane wave cutoff of 80 Ry is required. Given the small size of the unit cell, we use a K-point grid of  $4 \times 4 \times 2$  to sample the Brillouin zone. Based on these relaxed structures, we generated the corresponding supercells and calculated the defect formation energy for the tin vacancy in these mixed-cation systems, as reported in Table S2.

Defect quantities have been thus refined by using the hybrid HSE06 functional<sup>9</sup> ( $\alpha=0.43$ ) and DFT-D3 dispersions, by performing single point calculations at the PBE-D3 equilibrium geometries. Hybrid functional calculations have been carried out by using the same computational setup used for PBE calculation and reducing the cutoff on the Fock grid to 60 Ry, in order to reduce the computational effort. All DFT calculations have been performed by using the Quantum Espresso software package.<sup>10</sup>

The defect formation energies (DFE) and the thermodynamic transition levels (TTL) have been calculated by using the following equations[<https://doi.org/10.1063/1.1682673>]

$$DFE(X^q) = E(X^q) - E(perf) - \sum_i n_i \mu_i + q(E_f + V) + E^q(corr) \quad (1)$$

$$\varepsilon(q/q') = \frac{DFE(D^q, E_F = 0) - DFE(D^{q'}, E_F = 0)}{q' - q} + \frac{E_{corr}^q - E_{corr}^{q'}}{q' - q} \quad (2)$$

where  $E(X^q)$  is the energy of the supercell containing defect X,  $E(perf)$  is the energy of the non-defective system,  $n$  and  $\mu$  are, respectively, the number and the chemical potentials of the species added or subtracted to the non-defective system to form a defect;  $q$  is the charge of the defect. Long-range electrostatic interactions  $E_{corr}^q$  have been corrected through the Makov-Payne scheme by using the ionic dielectric permittivity of  $\text{MASnI}_3$  ( $\varepsilon=26$ ).

The chemical potentials of the atomic species have been set in order to simulate Sn-rich, Sn-medium, and Sn-poor conditions of growth, under the constraint of the thermodynamic stability of the  $\text{MASnI}_3$  and other phases. I-rich conditions:  $\Delta\mu_I = 0.0$  eV and  $\Delta\mu_{\text{Sn}} = -1.51$  eV; I-medium:  $\Delta\mu_I = -0.44$  eV and  $\Delta\mu_{\text{Sn}} = -0.75$  eV; and I-poor:  $\Delta\mu_I = -0.82$  eV and  $\Delta\mu_{\text{Sn}} = 0.0$  eV.

## Supporting Fig.s

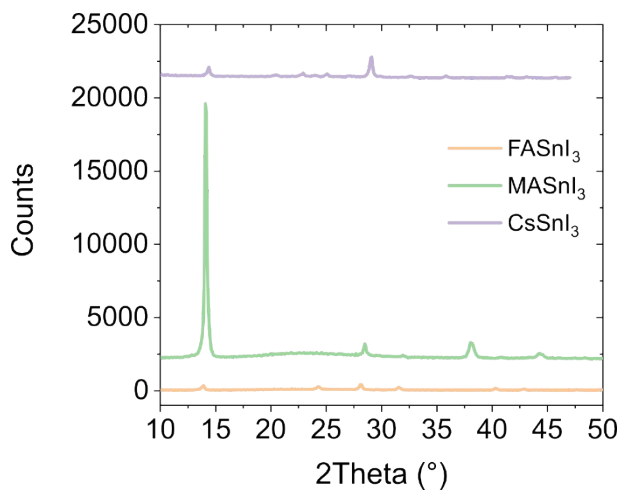


**Fig. S1.** XRD patterns of FASnI<sub>3</sub>, MASnI<sub>3</sub> and CsSnI<sub>3</sub> thin films.

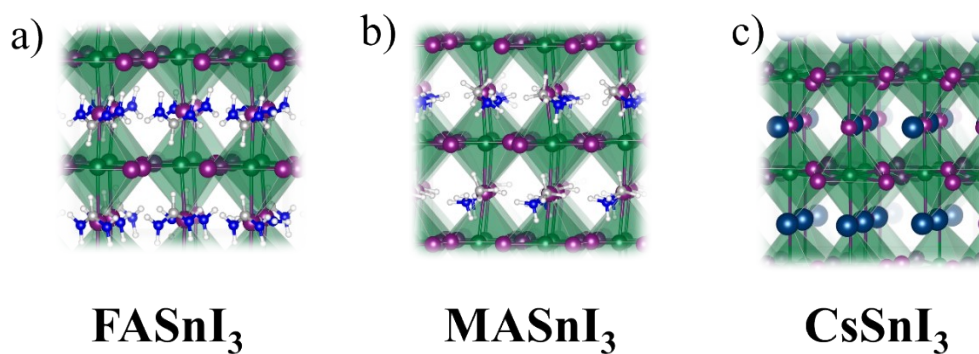


**Fig. S2.** Supercell structures of FASnI<sub>3</sub>, MASnI<sub>3</sub> and CsSnI<sub>3</sub>. Green is for tin, purple in for iodine.

**Table S1.** Cell parameters, Formation Energy ( $\Delta H_f$ ) and calculated Band gaps of FASnI<sub>3</sub>, MASnI<sub>3</sub> and CsSnI<sub>3</sub> at PBE-D3 and HSE06+D3 level of theory.

Cell parameters	FASnI <sub>3</sub>	MASnI <sub>3</sub>	CsSnI <sub>3</sub>
a (Å)	8.838	8.758	8.758
b (Å)	8.838	8.758	8.638
c (Å)	12.407	12.429	12.378
<b>Formation Energy <math>\Delta H_f</math> (eV)</b>			

PBE-D3	-0.027	-0.098	-0.28
HSE06-D3	-0.084	-0.152	-0.28
<b>Band Gap (eV)</b>			
PBE-D3	0.53	0.59	0.55
HSE06-D3	1.31	1.37	1.32

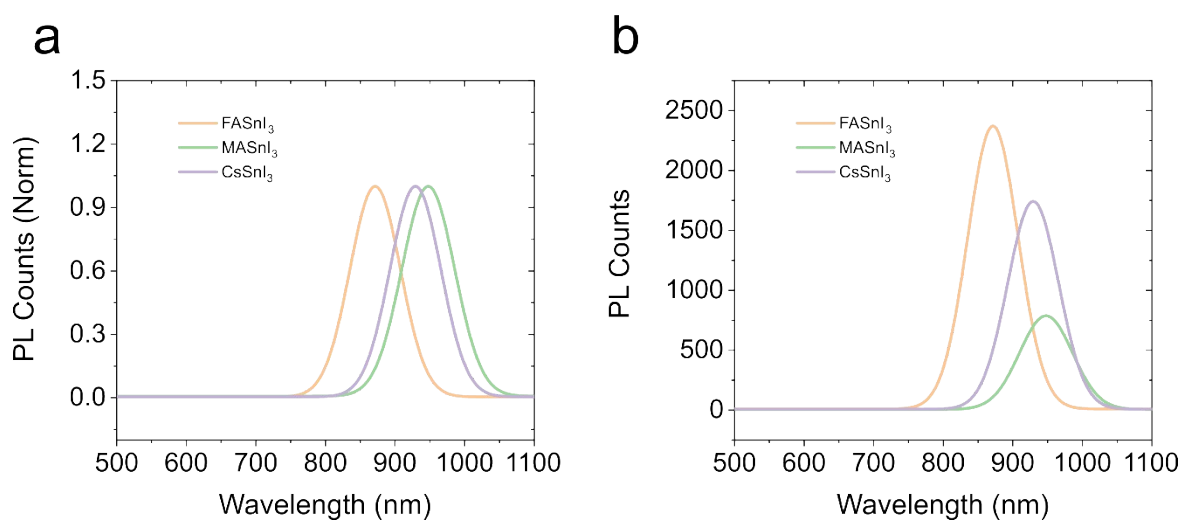


**Fig. S3.** Normalized and as measured PL peaks of FASnI<sub>3</sub>, MASnI<sub>3</sub> and CsSnI<sub>3</sub> thin films.

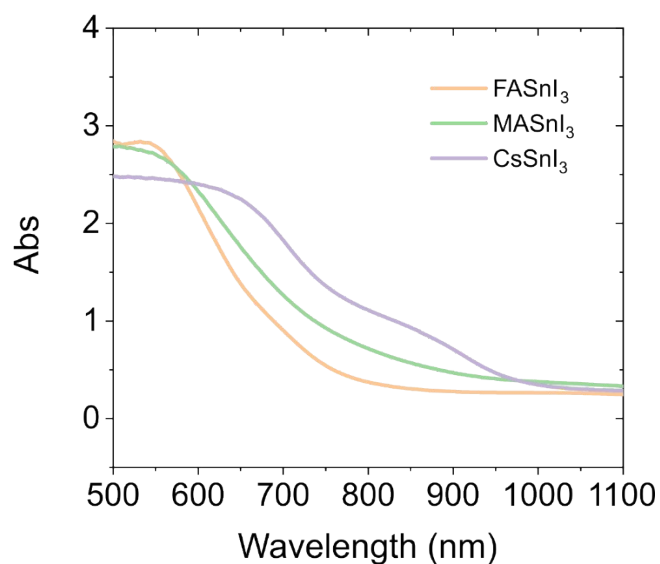


**Fig. S4.** UVVis absorption of FASnI<sub>3</sub>, MASnI<sub>3</sub> and CsSnI<sub>3</sub> thin films.

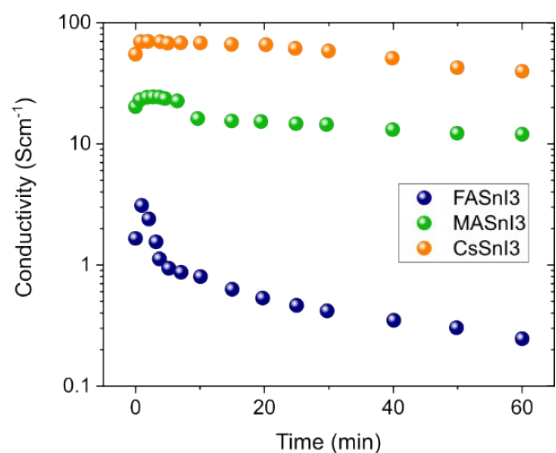


**Fig. S5.** Change in conductivity of non encapsulated FASnI<sub>3</sub>, MASnI<sub>3</sub> and CsSnI<sub>3</sub> thin films measured in air.

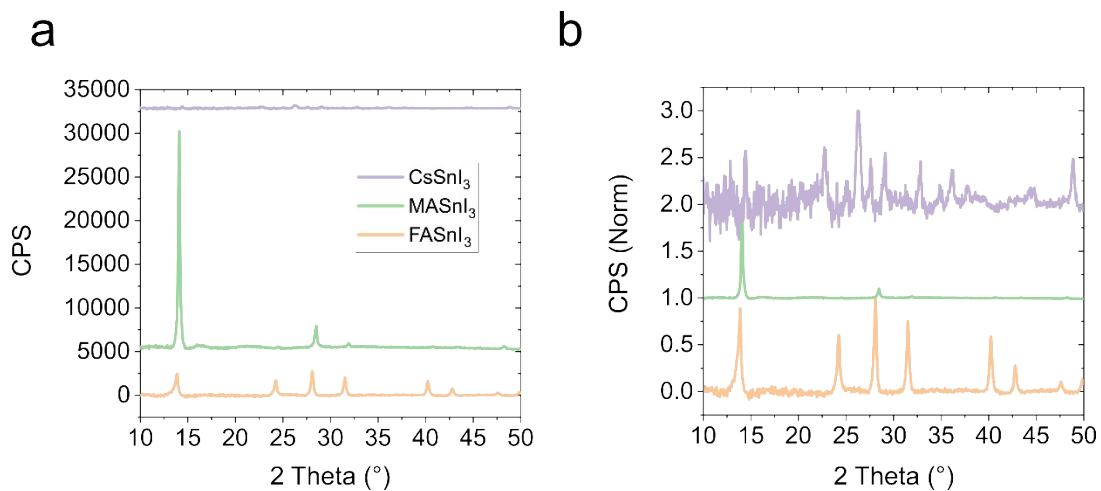


**Fig. S6.** Absolute (a) and normalised (b) XRD patterns of FASnI<sub>3</sub>, MASnI<sub>3</sub> and CsSnI<sub>3</sub> thin films without thermal annealing.

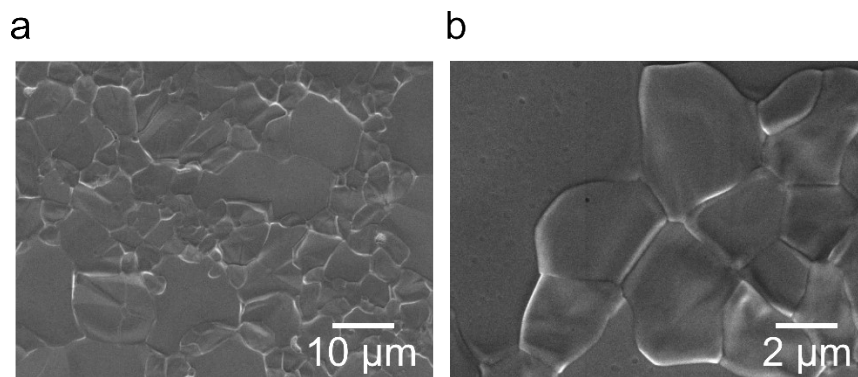


**Fig. S7.** Top-view SEM images of full coverage MASnI<sub>3</sub> films obtained using N<sub>2</sub> gas quenching procedure instead of the antisolvent (magnification of (a) 3 kx and (b) 15 kx).

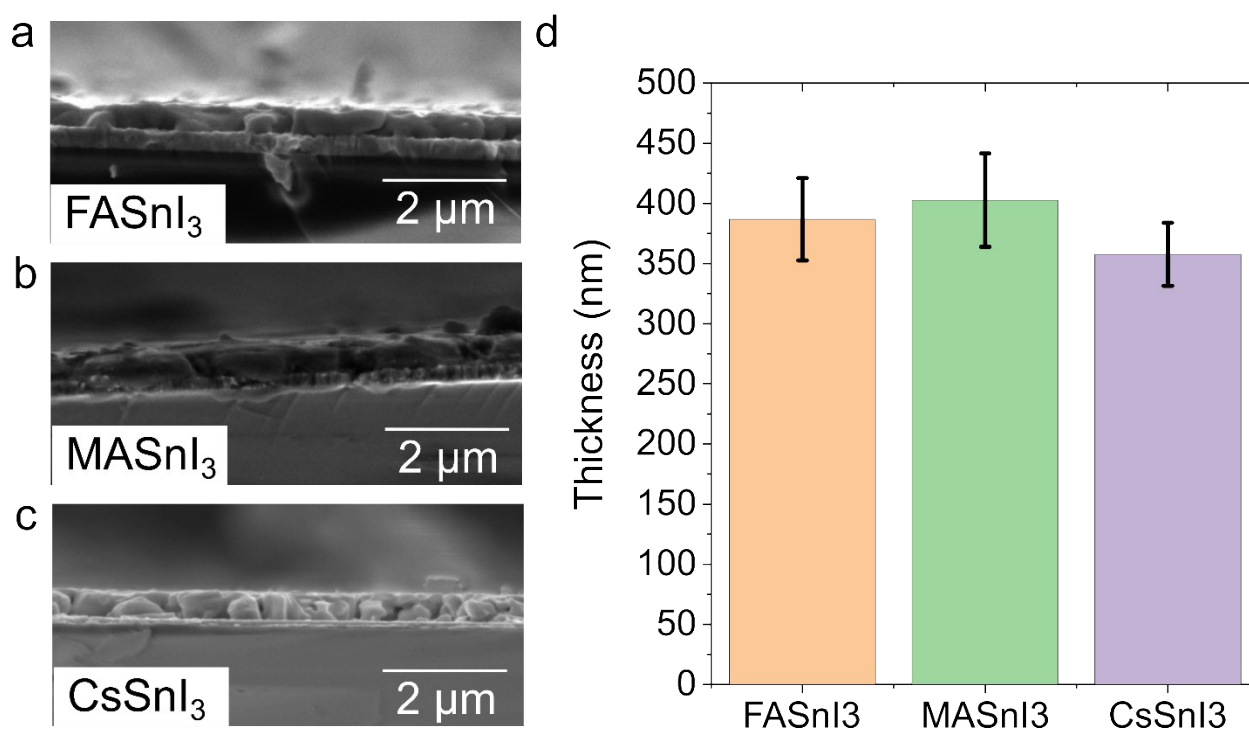


**Fig. S8.** Cross section SEM images of a. FASnI<sub>3</sub>, b. MASnI<sub>3</sub> and c. CsSnI<sub>3</sub>. d. Thicknesses of FASnI<sub>3</sub>, MASnI<sub>3</sub> and CsSnI<sub>3</sub> thin films estimated from cross-sectional SEM images.

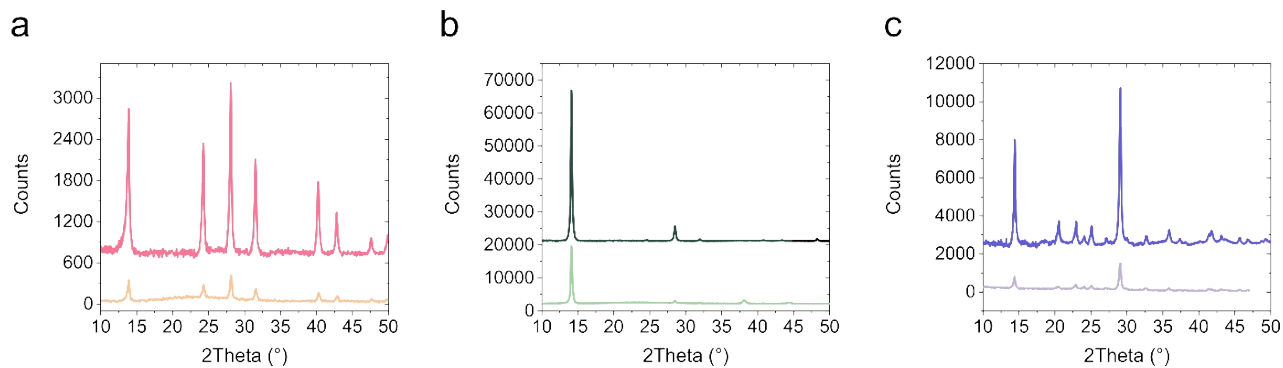


**Fig. S9.** XRD patterns of a) FASnI<sub>3</sub>, b) MASnI<sub>3</sub> and c) CsSnI<sub>3</sub> thin films before (bottom) and after (top pattern) optimization of the processing.

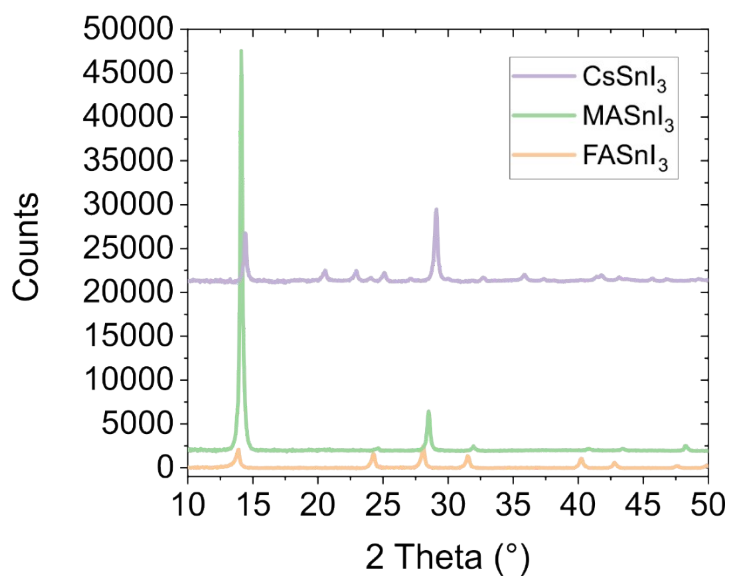


**Fig. S10.** Absolute intensity of XRD patterns of full coverage FASnI<sub>3</sub>, MASnI<sub>3</sub> and CsSnI<sub>3</sub> thin films (normalized values are showed in Fig 2d).

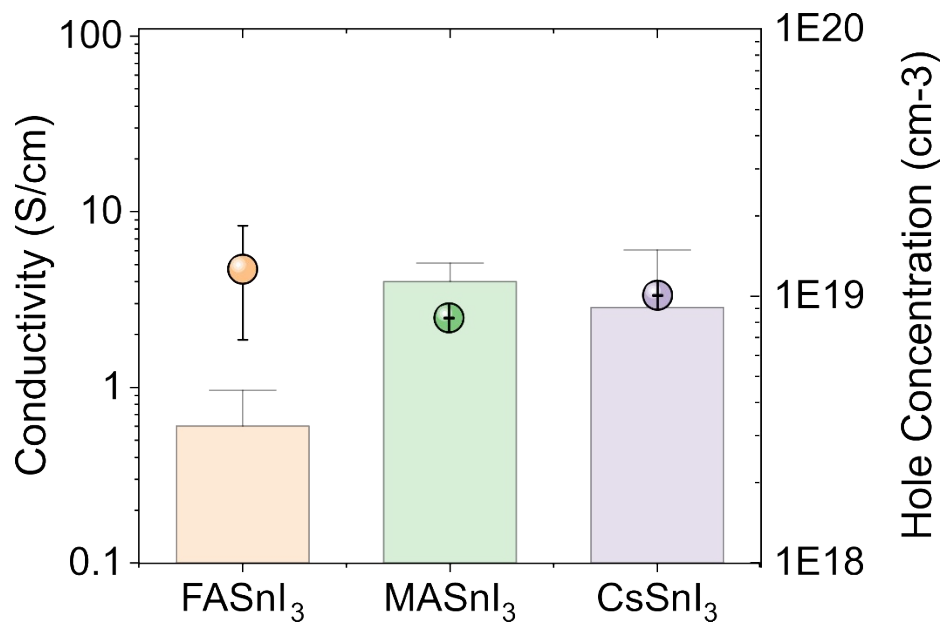


**Fig. S11.** Conductivity and doping density measured by Hall effect for FASnI<sub>3</sub>, MASnI<sub>3</sub> and CsSnI<sub>3</sub> spin coated thin films.

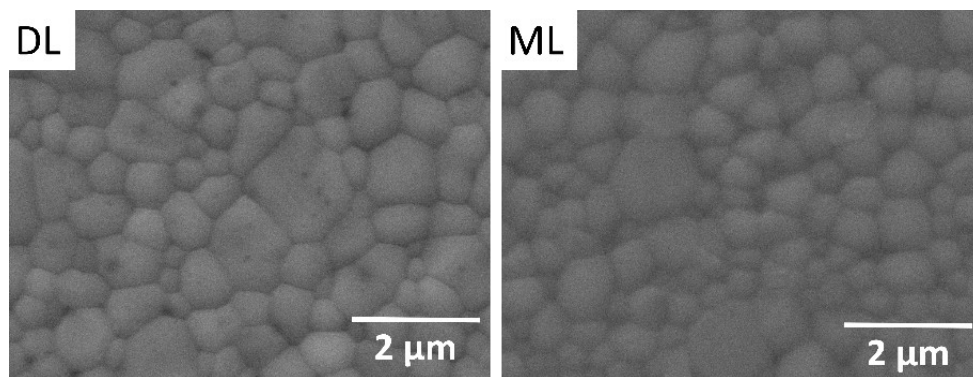


**Fig. S12.** Top view SEM images of thermally evaporated CsSnI<sub>3</sub> thin films obtained with double layer (DL) and multilayer (ML) approach.

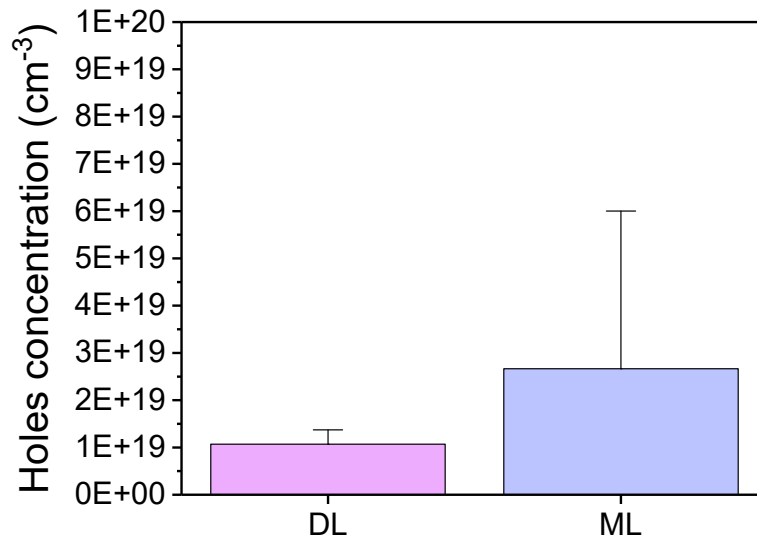


**Fig. S13.** Doping density obtained via Hall effect measurements for DL-type and ML-type thermally evaporated CsSnI<sub>3</sub> thin films.

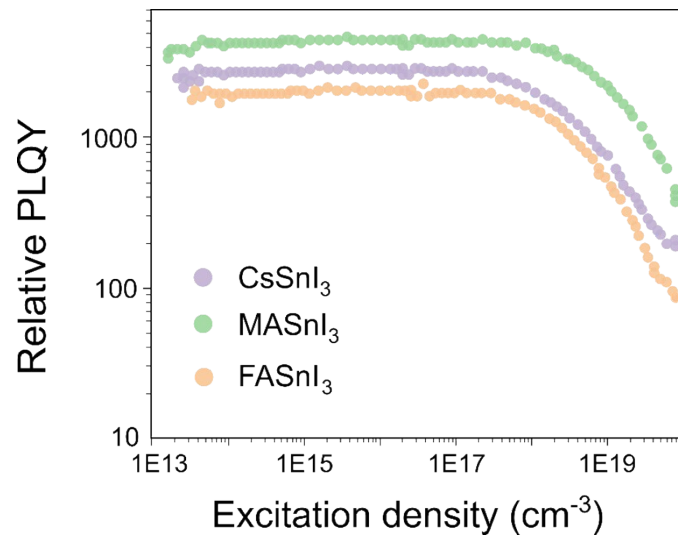
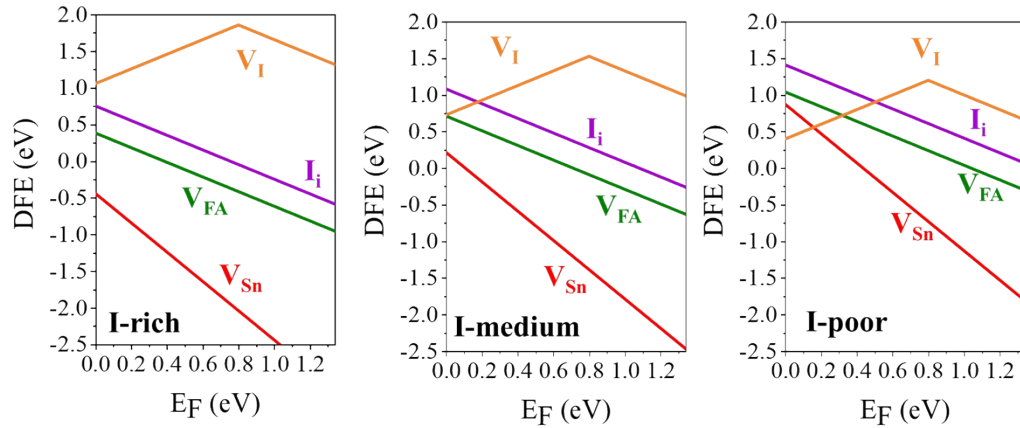
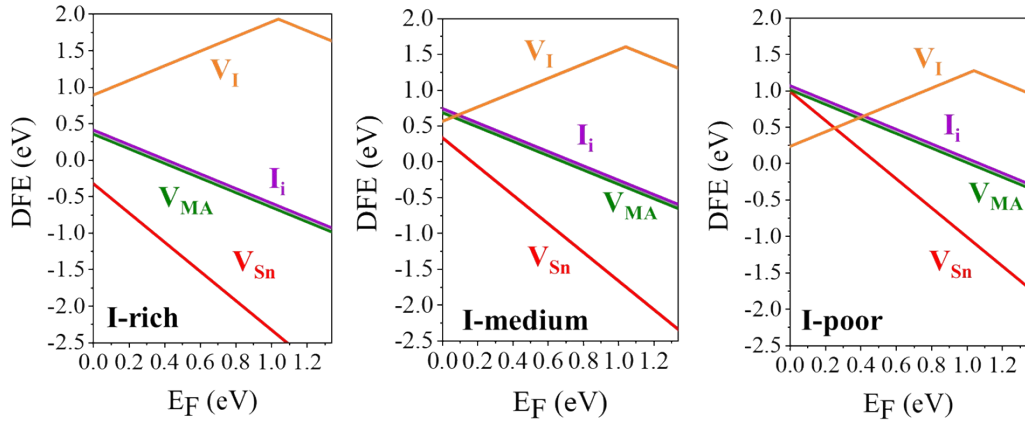


**Fig. S14.** Relative PLQY of FASnI<sub>3</sub>, MASnI<sub>3</sub> and CsSnI<sub>3</sub> thin films measured as a function of increasing excitation densities.

**FASnI3 (HSE06  $\alpha = 0.43$ )**



**MASnI3 (HSE06  $\alpha = 0.43$ )**



**CsSnI3 (HSE06  $\alpha = 0.43$ )**

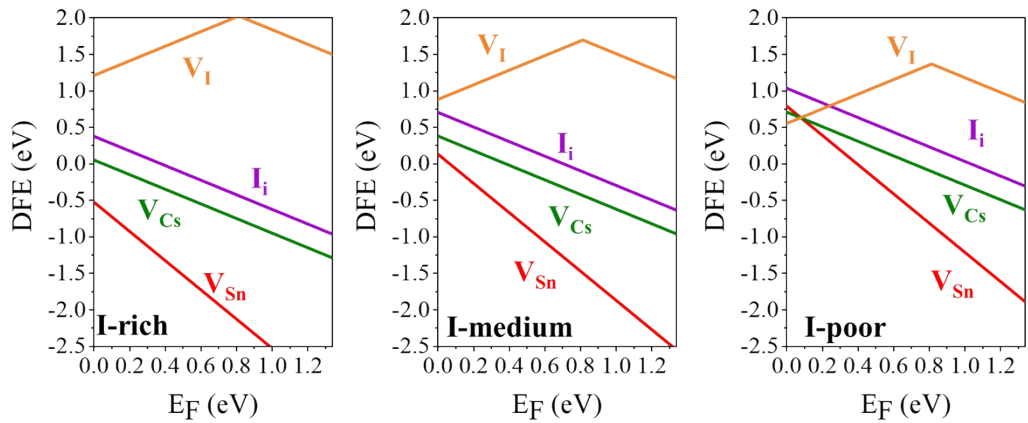


**Fig. S15.** Calculated DFEs of acceptor defects in different conditions of growth for the FASnI<sub>3</sub>, MASnI<sub>3</sub> and CsSnI<sub>3</sub> phases. DFE values are calculated at the HSE06-D3 level of theory.

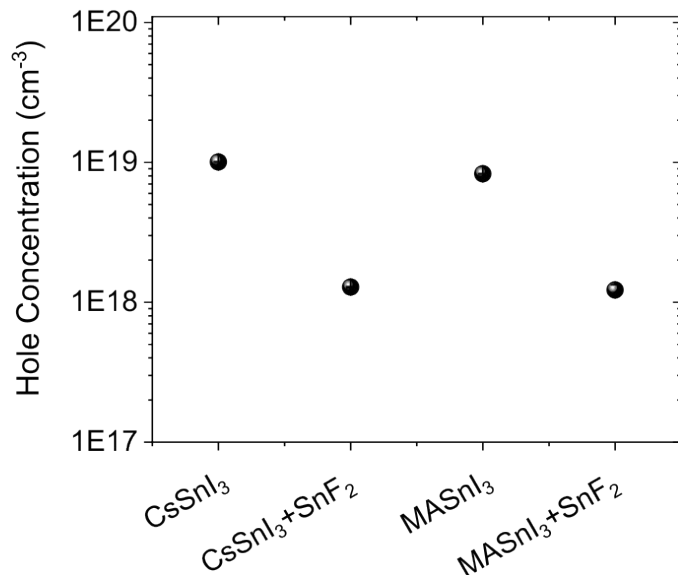


**Fig. S16.** Doping density measured by Hall effect for CsSnI<sub>3</sub> and MASnI<sub>3</sub> without and with addition of SnF<sub>2</sub>.

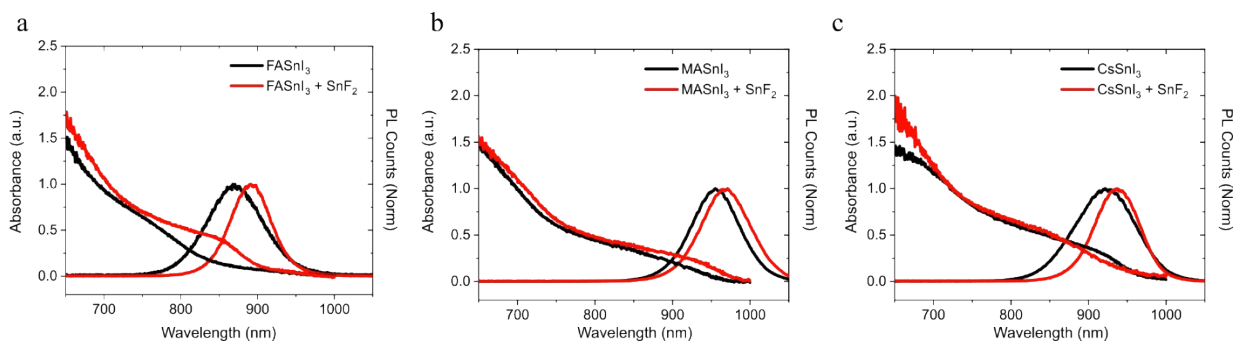


**Fig S17.** UV-Vis and PL spectra of a. FASnI<sub>3</sub>, b. MASnI<sub>3</sub> and c. CsSnI<sub>3</sub> thin films with and without 10 mol% of SnF<sub>2</sub>.

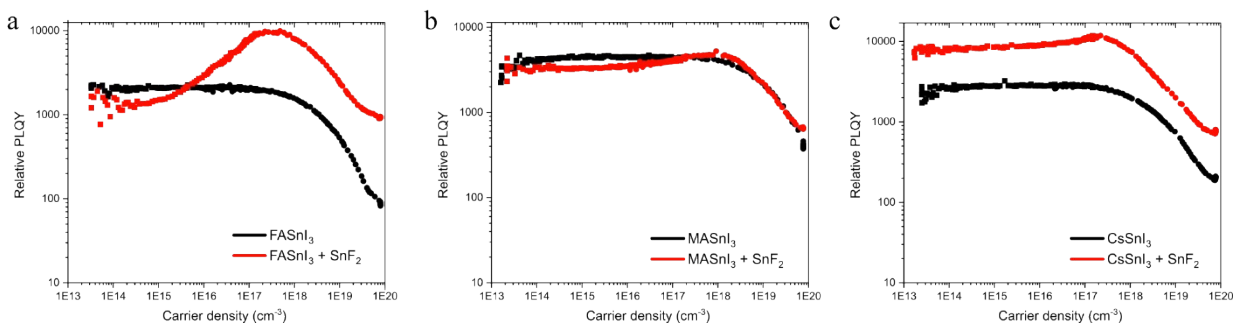


**Fig S18.** Relative PLQY of a. FASnI<sub>3</sub>, b. MASnI<sub>3</sub> and c. CsSnI<sub>3</sub> thin films without and with SnF<sub>2</sub> measured as a function of increasing excitation densities.

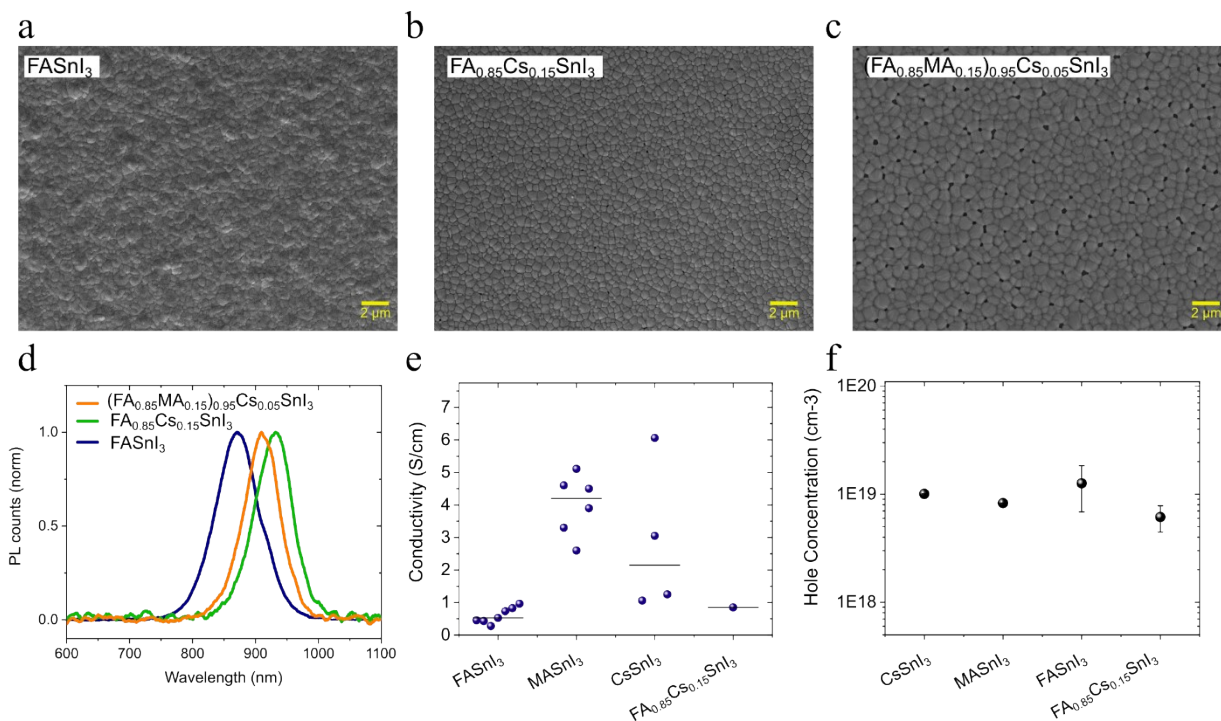


**Fig S19.** Top-view SEM images of a.  $\text{FASnI}_3$ , b.  $\text{FA}_{0.85}\text{Cs}_{0.15}\text{SnI}_3$  and c.  $(\text{FA}_{0.85}\text{MA}_{0.15})_{0.95}\text{Cs}_{0.05}\text{SnI}_3$ . d. PL spectra of  $\text{FASnI}_3$ ,  $\text{FA}_{0.85}\text{Cs}_{0.15}\text{SnI}_3$  and  $(\text{FA}_{0.85}\text{MA}_{0.15})_{0.95}\text{Cs}_{0.05}\text{SnI}_3$ . e. conductivity and f. hole concentration of  $\text{FASnI}_3$ ,  $\text{MASnI}_3$ ,  $\text{CsSnI}_3$  and  $\text{FA}_{0.85}\text{Cs}_{0.15}\text{SnI}_3$ .

**Table S2.** Calculated defect formation energies of the tin vacancy at the VBM in I-medium conditions and band gaps of  $\text{FASnI}_3$ ;  $\text{FA}_{0.75}\text{MA}_{0.25}\text{SnI}_3$  and  $\text{FA}_{0.75}\text{Cs}_{0.25}\text{SnI}_3$ . All the reported values have been calculated at the PBE level of theory.

	<b>DFE <math>\text{VSn}^{2-}</math> @VBM</b> <b>(eV)</b>	<b>Band gap</b> <b>(eV)</b>
<b><math>\text{FASnI}_3</math></b>	-0.66	0.60
<b><math>\text{FA}_{0.75}\text{MA}_{0.25}\text{SnI}_3</math></b>	-0.60	0.60
<b><math>\text{FA}_{0.75}\text{Cs}_{0.25}\text{SnI}_3</math></b>	-0.66	0.58

## References

1. Liu, J. *et al.* Lead-Free Solar Cells based on Tin Halide Perovskite Films with High Coverage and Improved Aggregation. *Angewandte Chemie* 130, 13405–13409 (2018).
2. Ternes, S., Laufer, F. & Paetzold, U. W. Modeling and Fundamental Dynamics of Vacuum, Gas, and Antisolvent Quenching for Scalable Perovskite Processes. *Advanced Science* 11, (2024).
3. Perdew, J. P., Burke, K. & Ernzerhof, M. Generalized Gradient Approximation Made Simple. *Phys Rev Lett* 77, 3865–3868 (1996).
4. Grimme, S., Antony, J., Ehrlich, S. & Krieg, H. A consistent and accurate ab initio parametrization of density functional dispersion correction (DFT-D) for the 94 elements H-Pu. *Journal of Chemical Physics* 132, (2010).
5. Stoumpos, C. C., Malliakas, C. D. & Kanatzidis, M. G. Semiconducting tin and lead iodide perovskites with organic cations: Phase transitions, high mobilities, and near-infrared photoluminescent properties. *Inorg Chem* 52, 9019–9038 (2013).
6. Chung, I. *et al.* CsSnI<sub>3</sub>: Semiconductor or metal? High electrical conductivity and strong near-infrared photoluminescence from a single material. High hole mobility and phase-transitions. *J Am Chem Soc* 134, 8579–8587 (2012).
7. Kahmann, S. *et al.* Negative Thermal Quenching in FASnI<sub>3</sub>Perovskite Single Crystals and Thin Films. *ACS Energy Lett* 5, 2512–2519 (2020).
8. van Setten, M. J. *et al.* The PSEUDODOJO: Training and grading a 85 element optimized norm-conserving pseudopotential table. *Comput Phys Commun* 226, 39–54 (2018).
9. Heyd, J., Scuseria, G. E. & Ernzerhof, M. Hybrid functionals based on a screened Coulomb potential. *Journal of Chemical Physics* 118, 8207–8215 (2003).
10. Giannozzi, P. *et al.* QUANTUM ESPRESSO: a modular and open-source software project for quantum simulations of materials. *Journal of Physics: Condensed Matter* 21, 395502 (2009).